Pergamon

Surface structure effects on direct reduction of iron oxides by *Shewanella oneidensis*

Andrew L. Neal,[1,2,*] Kevin M. Rosso,[3] Gill G. Geesey,[4,5] Yuri A. Gorby,[3] and Brenda J. Little[6]

[1]Department of Microbiology, University of Georgia, Athens, GA 30602, USA
[2]Savannah River Ecology Laboratory, University of Georgia, Aiken, SC 29802, USA
[3]Pacific Northwest National Laboratory, Richland, WA 99352, USA
[4]Biotechnology Department, Idaho National Engineering and Environmental Laboratory, Idaho Falls, ID 83415, USA
[5]Department of Microbiology, Montana State University, Bozeman, MT 59717, USA
[6]Oceanography Division, U.S. Naval Research Laboratory, Stennis Space Center, Starkville, MS 39529, USA

Abstract—The atomic and electronic structure of mineral surfaces affects many environmentally important processes such as adsorption phenomena. They are however rarely considered relevant to dissimilatory bacterial reduction of iron and manganese minerals. In this regard, surface area and thermodynamics are more commonly considered. Here we take a first step towards understanding the nature of the influence of mineral surface structure upon the rate of electron transfer from *Shewanella oneidensis* strain MR-1 outer membrane proteins to the mineral surface and the subsequent effect upon cell "activity." Cell accumulation has been used as a proxy for cell activity at three iron oxide single crystal faces; hematite (001), magnetite (111) and magnetite (100). Clear differences in cell accumulation at, and release from the surfaces are observed, with significantly more cells accumulating at hematite (001) compared to either magnetite face whilst relatively more cells are released into the overlying aqueous phase from the two magnetite faces than hematite. Modeling of the electron transfer process to the different mineral surfaces from a decaheme (protoporphyrin rings containing a central hexacoordinate iron atom), outer membrane-bound cytochrome of *S. oneidensis* has been accomplished by employing both Marcus and ab initio density functional theories. The resultant model of electron transfer to the three oxide faces predicts that over the entire range of expected electron transfer distances the highest electron transfer rates occur at the hematite (001) surface, mirroring the observed cell accumulation data. Electron transfer rates to either of the two magnetite surfaces are slower, with magnetite (111) slower than hematite (001) by approximately two orders of magnitude. A lack of knowledge regarding the structural details of the heme-mineral interface, especially in regards to atomic distances and relative orientations of hemes and surface iron atoms and the conformation of the protein envelope, precludes a more thorough analysis. However, the results of the modeling concur with the empirical observation that mineral surface structure has a clear influence on mineral surface-associated cell activity. Thus surface structure effects must be accounted for in future studies of cell-mineral interactions. *Copyright © 2003 Elsevier Ltd*

1. INTRODUCTION

Dissimilatory iron-reducing bacteria (including *Shewanella* spp., *Geobacter* spp. and *Ferribacterium* spp. inter alia) are afforded clear environmental significance in the cycling of iron (Nealson and Saffarini, 1995) due to reduction of Fe(III) associated with iron oxides/oxyhydroxides (Lovley, 1991) and clays (Kostka et al., 1996; Kostka et al., 1999), the reactivity of the resulting Fe(II) (Lovley et al., 1987; Fredrickson et al., 1998) and potential effects on the mobility of other metals and radionuclides (Landa et al., 1991; Nealson and Little, 1997). Solution chemistry effects upon biogenic Fe(III)-mineral reduction and subsequent precipitate formation have been intensively studied and, at least in laboratory reactors, are increasingly well understood aspects of the bioreduction process (Fredrickson et al., 1998; Zachara et al., 1998; Dong et al., 2000). However, a second factor with the potential to significantly influence the rate of Fe(III) reduction, namely iron-oxide mineral surface structure, has yet to be intensively studied.

A variety of iron oxides and oxyhydroxides are potentially available in anaerobic sediments to support dissimilatory iron-reduction including; goethite (α-FeOOH), lepidocrocite (γ-FeOOH), ferrihydrite ($Fe_5HO_8 \cdot 4H_2O$), hematite (α-Fe$_2$O$_3$)

and magnetite (Fe_3O_4) (Cornell and Schwertmann, 1996). Based upon abiotic reductive dissolution, phase reactivity is often assumed to follow the $Fe_5HO_8 \cdot 4H_2O \gg \gamma$-FeOOH $>$ $Fe_3O_4 > \alpha$-FeOOH $\geq \alpha$-Fe$_2$O$_3$ series (e.g., Sidhu et al., 1981; Canfield, 1989; dos Santos Afonso and Stumm, 1992). A similar series can be constructed based upon thermodynamic considerations (possibly of more relevance to bacterial growth), with γ-FeOOH and α-FeOOH at one extreme ($\Delta G^0_f = -477.7$ and -488.6 kJ mol^{-1} respectively), ferrihydrite, hematite and akaganéite (β-FeOOH) at intermediate free energy levels (-699, -742.7 and -752.7 kJ mol^{-1} respectively) and magnetite at the other extreme ($\Delta G^0_f = -1012.6$ kJ mol^{-1}) (Cornell and Schwertmann, 1996). Placed in context, only the reduction of ferrihydrite, γ-FeOOH and α-FeOOH is more thermodynamically favorable than sulfate ($\Delta G^0_f = -744.5$ kJ mol^{-1}) and thus these minerals are often considered the principle sources of ferric iron available to dissimilatory iron reducers in anaerobic sediments.

The sequence in reducibility described above has been demonstrated in cultures of Fe-reducing bacterial isolates from limnic sediments (Jones et al., 1983), anaerobic *Corynebacterium* cultures (Fischer, 1988) and *Shewanella putrefaciens* strain CN32 cultures (Zachara et al., 1998). Postma (1993) suggests a reactive continuum exists in natural iron oxide

---

* Author to whom correspondence should be addressed (neal@srel.edu).

assemblages, determined both by the intrinsic reactivity of the particular species and its surface area. In contrast, consideration of sedimentary pyritization and the likely principal authigenic iron phases has led Canfield et al. (1992) and Morse and Wang (1997) to suggest that surface area alone, which can range from 339 m^2 g^{-1} for ferrihydrite (Postma, 1993), to 19 m^2 g^{-1} and 17.5 m^2 g^{-1} for goethite and hematite respectively (Zinder et al., 1986; Banwart et al., 1989), not intrinsic reactivity (which they consider to be essentially the same for iron oxides), controls rates and thus the observed reducibility sequence. There is also a clear effect of crystallinity, with amorphous oxides being more readily reduced than crystalline phases (Munch and Ottow, 1980). It is apparent therefore that in any attempt to measure intrinsic susceptibility of iron oxides to biogenic reduction, the confounding effects of surface area and crystallinity must be accounted for.

Steps towards understanding the potential effect of surface area upon the rate and extent of iron reduction have been taken by Arnold et al. (1988), Roden and Zachara (1996) and Zachara et al. (1998), who demonstrate that both are positively correlated with surface area. However, separation of the influence of surface area upon mineral "reactivity" (that is to say the likely increase in reactive sites with increasing surface area) from the likely increase in the number of bacteria potentially able to attach to the surface (Das and Caccavo, 2000) remains unresolved. These studies also suggest that surface area alone does not control the rate of biogenic Fe-reduction since measured reduction rates of hematite samples of varying surface area by *Pseudomonas* sp. 200 (now known as *Shewanella putrefaciens* strain 200) do not agree with rates predicted solely on the basis of surface area (Arnold et al., 1988). Solid-phase structural considerations such as site-occlusion may also be important (Roden and Zachara, 1996) as well as the presence of structural defects (Rosso et al., 2003b).

Clearly, any consideration of the likely control that surface structure plays in determining rates of iron reduction must necessarily take into account the principal mechanism by which iron reduction is achieved. Currently there exist two predominant mechanisms by which bacteria are thought to accomplish electron transfer (ET) to crystalline iron oxides: enzymatic, whereby outer membrane based cytochromes are responsible for the direct transfer of electrons to the mineral surface, and shuttle compounds. Many metal reducing bacteria have been found also to be capable of reducing humic acids (Lovley et al., 1998), often substituted by anthraquinone-2,6-disulfonate (AQDS) in laboratory experiments. AQDS as well as other quinone containing moieties and pyomelanin (Newman and Kolter, 2000; Turick et al., 2002) are suggested possible electron shuttles between bacteria and crystalline mineral surfaces, thereby circumventing the necessity for direct contact between the bacterial outer membrane and the mineral (e.g., Rosso et al., 2003b). The fact that humic acids are able to act as terminal electron acceptors in bacterial anaerobic respiration (Lovley et al., 1996) means the question ceases to concern bacterial iron reduction per se. The extent of ferrihydrite reduction is positively correlated with cell attachment of *Shewanella* (Das and Caccavo, 2000), and specific interactions between *Shewanella* cell surfaces and iron oxides have been observed (Lower et al., 2001); these observations provide compelling evidence for surface associated ET. Given that shuttling of electrons in flowing systems remains undocumented, we have chosen to model the direct, enzymatic reduction via outer membrane-bound cytochromes. In addition, this approach has the added advantage of tackling a relatively less complex system—direct ET versus the consideration of an intermediate shuttle compound. And finally, we note that because the focus of this study is the oxide electron acceptor and how its surface structure affects microbial activity, the only requirement placed on the electron donor species is that it be common to all systems under consideration.

The confounding effect of surface area can presumably be overcome by studying growth rates/dissolution rates of single crystal faces of various iron oxides. To our knowledge, bioreduction experiments on well-defined single crystalline oxide surfaces have not been reported. In this study, we attempt to address a key issue in the surface area problem by employing a series of three single crystal iron oxide surfaces for comparison of bioreduction rates, namely hematite (001), magnetite (111), and magnetite (100). The structures of the three surfaces are expected to differ significantly for many reasons, not the least of which is that whilst hematite possesses the corundum structure and has univalent iron (α-Fe_2O_3), magnetite possesses the inverse spinel structure and has mixed-valent iron ($[Fe_2^{2+}$, $Fe^{3+}]O_4$). Additionally, the three surfaces exhibit a range of Fe(III) site densities and therefore the sheer numbers of electron accepting sites occurring in the near surface region are expected to be different. Therefore, under the assumption that the rate of the terminal ET step between a microorganism and oxide surface impacts the activity of the cell, it is reasonable to hypothesize that oxide surface structure should play an important role.

In this study, we investigate the effects of oxide surface structure on the activity of *Shewanella oneidensis* MR-1 using a combined experimental and theoretical approach. Anaerobic cell growth on the three well-characterized single crystalline iron oxide surfaces in flow reactors was monitored and used as a proxy for bioreduction activity. A combination of ab initio modeling and Marcus theory is used to predict ET rates from a model outer-membrane bound cytochrome molecule to the three different oxide surfaces, and to evaluate the principal structural and energetic factors that lead to intrinsic differences in the surfaces as electron acceptors for bioreduction.

2. MATERIALS AND METHODS

2.1. Iron Oxide Minerals

Natural single crystals having well developed specific crystallographic faces were used for the experiments in this study. Single crystal growth faces were used in all experiments. Hematite (001) faces were isolated on specular tabular hematite from Brazil acquired from the Stanford Mineralogical collection (sample 51080). Magnetite (100) faces were isolated on tetrahexahedrons from New York, acquired from the Harvard Mineralogical Collection (sample 134816). Magnetite (111) faces were isolated on octahedrons from Vermont, acquired from the Harvard Mineralogical Collection (sample 93.1.5.2). Clean, flat, stoichiometric growth faces were identified using multi-scale atomic force microscopy (AFM) and X-ray photoelectron spectroscopy (XPS, described below in section 2.8). AFM measurements were performed with the samples under Milli-Q water at ambient conditions using a Digital Instruments, Inc. BioScope operating in contact mode. Imaging in water improved image resolution, likely by eliminating capillary forces that are often present between the tip and sample in air due to the presence of adsorbed water overlayers. Standard Si_3N_4 probes were
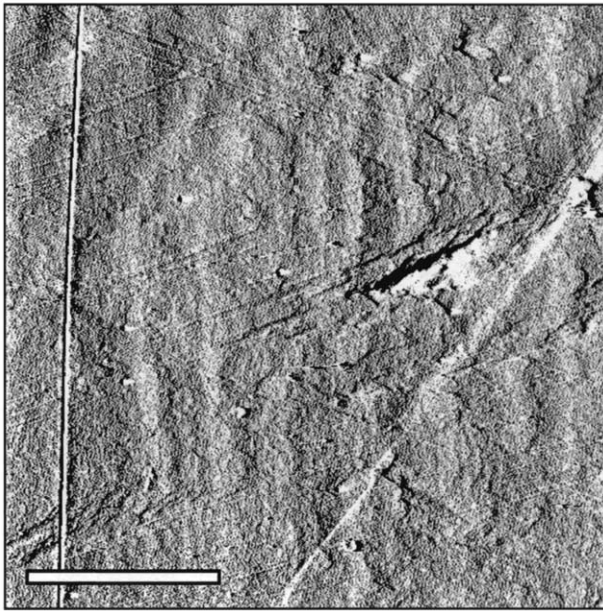
Fig. 1. Contact mode atomic force micrograph showing typical features found on the as-is growth surface of our samples of magnetite (100). The scale bar is 4 μm. The image data is from the deflection signal. Secondary phases are generally absent and surface topographic relief possesses minimal amplitude. The root-mean-square roughness over the entire image area is only 1.4 nm. These attributes are representative for the series of three surfaces used in this study.

used, having a nominal radius of curvature of 20–60 nm and an approximate spring constant of 0.12 N m^{-1} for the chosen cantilever. Scan rates varied between 0.5–1.0 Hz. AFM showed that the surfaces were replete with areas ideal for our experiments because of their size (several tens of microns in lateral extent) and because they had very little surface microtopography and a negligible presence of secondary phases (Fig. 1). XPS of the Fe 2p lines was used to confirm the proper stoichiometry at the surfaces of magnetite in particular, to ensure the surfaces had not oxidized to maghemite.

2.2. Description of Bacterial Strain

The facultative iron-reducing bacterium *Shewanella oneidensis* strain MR-1 (ATCC 700550, formerly identified as *S. putrefaciens* MR-1, Venkateswaran et al., 1999) was used in the experiments described here. The organism as used in our laboratory contains Green Fluorescent Protein (GFP) encoded on a p519nGFP plasmid which also confers resistance to the antibiotic kanamycin. Since enumeration of cells at the mineral surfaces was based upon epifluorescent imaging (see section 2.5) it was necessary to ensure that only cells capable of GFP production were present at the surfaces. Therefore, to ensure that only those *S. oneidensis* cells containing the plasmid (and capable of GFP production) were present, all cells were cultured in media containing 100 μg mL^{-1} kanamycin. This concentration has been determined to be the lowest at which no plasmid-free cells grow.

2.3. Culture Conditions

Shewanella oneidensis MR-1 was cultured anaerobically in a defined medium adapted for optimum anaerobic growth (M1, Kostka and Nealson, 1998). Besides 32 mM lactate which served both as carbon source and electron donor M1 contains 9 mM $(NH_4)_2SO_4$, 6 mM K_2HPO_4, 3.3 mM KH_2PO_4, 2 mM $NaHCO_3$, 1 mM $MgSO_4$, 0.5 mM $CaCl_2$, 67.2 μM Na_2EDTA, 56.6 μM H_3BO_3, 10 μM NaCl, 5.4 μM $FeSO_4$, 5 μM $CoSO_4$, 5 μM $Ni(NH_4)_2SO_4$, 3.9 μM Na_2MoO_4, 1.5 μM Na_2SeO_4, 1.3 μM $MnSO_4$, 0.2 μM $CuSO_4$, 20 mg L^{-1} arginine, 20 mg L^{-1} serine and 20 mg L^{-1} glutamic acid. For batch cultures 40 mM

Fe(III)-citrate (stock adjusted to pH 7 with 10 N NaOH) was added as electron acceptor. For flow reactor studies Fe(III)-citrate was omitted, thus the only electron acceptor available was the solid phase mineral sample. All media were sparged using O_2-free N_2 before heat sterilization. Fe(III)-citrate and kanamycin solutions were added aseptically (filter sterilized, 0.2 μm) to sterile medium. Batch cultures (100 mL) were grown in anaerobic flasks using butyl rubber septa and aluminum crimp caps (Wheaton, Millville, NJ) at 30°C. Larger volumes of sterile medium required for flow reactor experimentation were stored in 750 mL anaerobic flasks (Wheaton).

2.4. Flow System and Reactor

All experiments were performed at room temperature (22–24°C) in a laboratory-designed anaerobic flow reactor (external dimensions 100 $\times$ 72 $\times$ 14 mm, length $\times$ width $\times$ height) constructed of Teflon™. The effective chamber dimensions are 48 $\times$ 12 $\times$ 0.8 mm, the floor of which has two recesses (10 $\times$ 10 mm) to hold mineral samples set in Spurr low viscosity epoxy resin (Polysciences Inc., Warrington, PA). A cover glass (24 $\times$ 60 mm), sealed against the Teflon chamber with an oversize Viton gasket and aluminum coverplate, acts as viewing window. Near pulse-free flow is achieved using a reciprocating syringe pump (KDS210, KD Scientific, New Hope, PA) equipped with two 50 mL Microtite syringes (Popper & Sons Inc., New Hyde Park, NY) operating at 30 μL min^{-1} (chamber flow velocity = 3.2 $\times$ 10^{-2} cm s^{-1}). All tubing (internal diameter 1016 μm, wall thickness 560 μm) and fittings are constructed of PEEK (Upchurch Scientific, Oak Harbor WA) chosen for its superior oxygen impermeability. The sterile medium reservoir was continuously sparged with N_2 to maintain anaerobic conditions. Preliminary experiments using oxygen microelectrodes suggest that oxygen concentrations within the flow reactor are below the sensitivity of such electrodes.

All surfaces were inoculated with an overnight batch culture grown at 30°C with 40 mM Fe(III)-citrate as the electron acceptor. The flow system was cleaned, sterilized and re-used for each trial with the effect that internal surface area was kept constant minimizing both inter and intratrial variability. The underlying assumption was thus that any observed differences in cell density and detachment rates were a product of the varying surface properties, not simply due to differences in potential numbers of cells attached upstream of the mineral surfaces which would provide a greater potential number of surface colonizers.

2.5. Microscopy and Image Analysis

Observation of MR-1 attached to the various mineral faces was made using an Olympus BX60 microscope equipped with an infinity-corrected, long working distance water immersion objective lens (40$\times$, NA = 0.8, Olympus America Inc., Lake Success, NY) and 100 W Hg-vapor discharge lamp. Reflected differential interference contrast (DIC) images were captured using a U-DICR polarizer (Olympus America Inc.), fluorescence images with a WIBA filter block (460–490 nm excitation; 505 nm dichroic mirror; 515–550 nm emission; Olympus America Inc.). Video capture was performed using an ImagePoint monochrome, Peltier cooled (+10°C) CCD camera (Photometrics Ltd., Tucson, AZ) and Image-Pro Plus software (Media Cybernetics, Silver Springs, MD). Cell density was assessed using analysis of captured epifluorescent images of randomly chosen areas on the surface.

2.6. Surface-Associated Cell Accumulation

S. oneidensis cell accumulation data combined from two trials on each mineral face was successfully described using an exponential sigmoid curve of the type

$$\{(b + a) + (b - a) \cdot (1 - \exp(k \cdot abs(X - X_{50}))) \cdot sign(X - X_{50})\} \cdot 0.5 \quad (1)$$

where a = minimum and b = maximum cell densities (cells cm^{-2}). From this curve, an estimate of the rate of cell accumulation (μ, cells cm^{-2} min^{-1}) was derived according to Eqn. 2:

$$\mu = ((b - a)/2) \cdot k \quad (2)$$

The standard error of μ (SE_μ) for the combined data sets was estimated using a Taylor series approximation (Casella and Berger, 1990);

$$SE_\mu = \sqrt{(k^2[((\text{var}(a) + \text{var}(b)) - 2\text{cov}(a,b))/4] + [\mu^2(\text{var}(k)/k^2)] + [\mu/2(\text{cov}(b,k)) - (\text{cov}(a,k))])} \qquad (3)$$

2.7. Collection and Enumeration of Detached Cells

During one trial on each crystal face, detached cells were collected at the out-flow. Planar crystal phase surface areas for these trials were measured to be 0.62 cm^2 for hematite, 0.71 cm^2 for magnetite (100) and 0.68 cm^2 for magnetite (111). Cells were collected directly into a chilled fixative solution containing a final 2% concentration of formaldehyde in a phosphate buffered saline (PBS, pH 7.2) solution (Vives-Rego et al., 2000). Following 12 h incubation at 4°C, cells were harvested by centrifugation, washed in a 0.01% solution of a nonionic detergent (IGEPAL CA-630, Sigma Chemical Co., St. Louis, MO) in PBS and finally placed in a 50:50 solution of storage buffer containing 10 mM Tris buffer (pH 7.2), 0.1% IGEPAL CA-630 and 96% ethanol. This fixation step ensured cell integrity for flow cytometry. Samples were stored at 4°C until further use. Enumeration of cells was performed with a FACSCalibur flow cytometer (Becton Dickinson Immunocytometry Systems, San Jose, CA). Before measurement samples were briefly mixed via sonication to ensure that cells were not clumped (Nebe-von Caron and Badley, 1996).

The instantaneous cell detachment rate, $D(t)$ (cells min^{-1}), was calculated in a similar fashion to that described by Baty et al. (2000):

$$D(t) = (N_e)_{t=n}(V_{t=n-1})/t_{n-1} \qquad (4)$$

where $(N_e)_{t=n}$ is the cell concentration in the effluent (cells mL^{-1}) at time n, $V_{t=n-1}$ is the volume (ml) that passed through the flow cell since the previous measurement ($n - 1$) and t_{n-1} is the elapsed time (min) since the previous measurement.

To account for alternative (O$_2$) electron acceptor-dependent mineral surface-associated cell production and accumulation, cell densities were determined on silicon surfaces under otherwise identical conditions of growth medium and flow rate. Silicon does not act as a terminal electron acceptor for dissimilatory iron reducing bacteria.

Having established the numbers of cells attached to the respective mineral faces at each time point, and the total number of cells recovered from the effluent and therefore detached from the surface, an assessment of total cell productivity (P) for each face as a function of time was made using

$$P = \sum_{n=1}^{1} (N_n - N_{n-1} + N'_n) \qquad (5)$$

where N_n is the number of cells on the surface (cell density x surface area) and N_n' is the cell count in the effluent at time n. Thus, the total productivity is defined as the change in the number of cells on the surface added to the cell count in the effluent at each time point, and this quantity is summed cumulatively over time.

2.8. X-Ray Photoelectron Spectroscopy

X-ray photoelectron spectroscopy (XPS) was employed to determine the valence state of Fe on uncolonized and colonized iron oxide surfaces providing confirmation that Fe-reduction had occurred at the mineral surface in the presence of *S. oneidensis* cells. Spectra were collected on a Perkin-Elmer Physical Electronics Division Model 5600ci spectrometer (Perkin Elmer Inc., Eden Prairie, MN). The spectrometer was calibrated employing the Au$4f_{7/2}$, Cu$2p_{3/2}$ and Ag$3d_{5/2}$ photopeaks with binding energies of 83.99, 932.66 and 368.27 eV respectively. A consistent 800 μm spot size was analyzed on all surfaces using a monochromatized AlK_α (hν =1486.6 eV) X-ray source at 300 W and a pass energy of 46.95 eV for survey scans, and 11.75 eV for high-resolution scans. The system was operated at a base pressure of 10^{-8}-10^{-9} torr. A consistent emission angle was used ($2\theta = 45°$). Valence states were analyzed applying multiplet-splitting models derived for the $2p$ photopeaks of the Fe(III) and Fe(II) ions by Gupta and Sen (1974, 1975). The applicability of these models to resolving contributions to the $2p$ photopeak from the two ions has been demonstrated (McIntyre and Zetaruk, 1977; Pratt et al., 1994a,b; Herbert et al., 1998; Neal et al., 2001). Peaks were fitted using a 70: 30 gaussian: Lorenztian peak shape and a constant full width at half maximum. By indexing the binding energy shift and intensity of each multiplet peak to the principal peak for the respective ion, the fitting procedure is simplified, only those parameters pertaining to the principal peaks need be adjusted iteratively. All peak fitting was preceded by baseline subtraction employing the Shirley algorithm (Shirley, 1972).

Following reactor operation for 10 d, mineral samples were recovered under an anaerobic (95% N$_2$-5% H$_2$) atmosphere for spectroscopic analysis (details described below). Samples were wicked dry with a tissue, and mounted on a stub and held in place with a shield for X-ray photoelectron spectroscopy (XPS). The mounted samples were transported to the spectrometer in a chamber containing a dry AnaeroPack system (Mitsubishi Gas Chemical America Inc., New York, NY) to minimize (less than 5 s) exposure of the sample to the ambient atmosphere between the time the sample was mounted and introduced into the XPS spectrometer, which contained a N$_2$ atmosphere.

2.9. Theoretical Treatment of Heterogeneous ET Rates

We modeled the kinetics of the terminal step of direct enzymatic reduction of the different iron oxide mineral surfaces using a combination of Marcus theory, ab initio density functional theory (DFT) calculations, knowledge of the mineral surface structures, and generalized characteristics of a model outer membrane Fe(III)-reductase for *Shewanella*. The model applied here is an adaptation of a previously established model for homogeneous ET (Rosso and Rustad, 2000; Rosso and Morgan, 2002; Rosso et al., 2003a) for the current case of heterogeneous ET across an interface. Many of the details of our modeling strategy can be gleaned from Rosso et al. (2003a) and Eggleston et al. (2003), thus, only details pertinent to the model adaptation used here are discussed below. For general introductions to electron transfer theory, the reader is referred to Newton and Sutin (1984) and Marcus and Sutin (1985).

The molecular-level structure, properties, and surrounding environment of cytochromes functioning as terminal reductases under the true conditions of direct ET at the cell/mineral interface are very poorly understood. The foremost purpose of the modeling aspect of this study is to differentiate between the intrinsic electron accepting properties of the three different oxide surfaces. To do this demands little exact knowledge of the properties of the electron donor, except that it is common to the three surfaces, but comprehensive knowledge of the properties of the mineral surfaces. Thus, with regards to the electron donor, whether or not we have chosen the correct cytochrome properties or even the cytochrome itself is unimportant. Whilst outer membrane-bound proteins are understood to be required for Fe(III) reduction to occur, few details on their elementary ET reactions are available and none are available specific for the ET conditions in this study. Several cytochromes have been identified as possible terminal iron reductases for *Shewanella* including OmcA (Myers and Myers, 1998, 2001) and MtrC (Beliaev et al., 2001). Both are decaheme c-type cytochromes. As it bears little impact on the conclusions of this study, we have chosen OmcA as the model cytochrome for rate calculations with the various iron oxide surfaces. In addition, as described below, the ET properties we assign to OmcA are a synthesis of experimental findings on purified OmcA and experimental and theoretical properties of heme groups in c-type cytochromes.

Because the considered ET is between fixed and oriented sites from a cytochrome heme center at some fixed distance from the oxide surface, the reaction is formally one of first-order. It is also assumed to occur as a "through-space" ET reaction (outer-sphere), rather than "through-bond" via a bridging ligand (Marcus and Sutin, 1985). Because of the physics of electron conduction in hematite and magnetite, which follows the small polaron model (Goodenough, 1971; Sherman, 1987; Rosso et al., 2003a), electrons injected into these minerals couple with a small lattice distortion and together can be treated as localized quasi-particles, rather than as delocalized in the conduction bands. In the latter case, total ET rates to the surface are usually based on a summation over the continuum of electronic states in the conduction

band (e.g., Gao et al., 2000). In our case, the total ET rate k is taken as a summation overall possible Fe(III) acceptor sites n in the near surface region for a given location of the donor heme center of the cytochrome molecule, given by:

$$k = \sum_{i=1}^{n} x_i m_i k_i \qquad (6)$$

where m is the multiplicity of symmetrically equivalent nominally Fe(III) sites and k is the fraction of those sites in the 3^+ valence state at any given time (pertaining to the $2^+/3^+$ charge balance that must be maintained in the octahedral Fe sublattice in magnetite).

Electron transfer distances between a heme center in a membrane-bound cytochrome and Fe(III) sites in the oxide surfaces are expected to be relatively large (see Results section). Thus, it is likely that electronic interaction between them is rather weak (Marcus and Sutin, 1985). To reflect this, we have chosen the non-adiabatic (weak-mixing) approximation for the rate expression. The first order rate constant for a single non-adiabatic ET step k^{et} is given by:

$$k^{et} = \frac{2\pi}{\hbar} H_{AB}^2 \frac{e^{-(\Delta G^{\circ\prime}+\lambda)^2/4\lambda RT}}{\sqrt{4\pi\lambda RT}} \qquad (7)$$

where $\hbar$ is Planck's constant, H_{AB} is the electronic matrix element describing the coupling of the electronic state of the reactants to that of the products, $\Delta G^{\circ\prime}$ is the free energy change for the electron transfer reaction, λ is the energy to reorganize the nuclear coordinates of the reactants and surrounding solvent molecules into the configuration consistent with electron transfer, R is the gas constant, and T is the temperature (taken as 298.15 K throughout this study) The configuration appropriate for electron transfer is that in which the electronic state of the reactants is equivalent to that of the products. Achieving this coincidence condition is usually discussed in terms of two possibilities. The structure of the reactants can be distorted into the configuration of the products, by optical excitation for example, in effect vertically exciting the reactants by the energy λ into the electronic state of the products. Alternatively, coincidence can be achieved via an intermediate crossing point, a transition state between the reactants and products states. This normal pathway for thermally promoted electron transfer is modeled here. The energy of the transition state is the activation energy (ΔG^*). For ET reactions requiring only small displacements in nuclear coordinates, the reactants and products potential energy surfaces are well described by parabolas and ΔG^* is easily determined from knowledge of λ and $\Delta G^{\circ\prime}$ (Marcus, 1956). The electronic coupling term H_{AB} represents the interaction between reactant and product states in the transition state configuration. For more detailed explanations of these parameters relevant to the current system see Rosso et al. (2003a).

The atomic structures of hematite and magnetite surfaces in water are poorly understood. Many reconstructions and vacancy structures have been proposed for both magnetite faces based upon experiments performed in ultra-high vacuum environments as well as theoretical modeling. While several surface atomic arrangements are available, definitive fully relaxed atomic coordinates are lacking. We adopt the (1×1) magnetite (111) termination of Ritter and Weiss (1999) and the $(\sqrt{2} \times \sqrt{2})$ magnetite (100) termination of Chambers et al. (2000) since these represent the simplest cases (no reconstruction) and are the most electrostatically stable structures for those terminations (Fig. 2). The former surface is terminated by a 1/4 monolayer of tetrahedral Fe atoms, the latter by a 1/2 monolayer of tetrahedral Fe atoms. Hematite (001) can be either Fe or O(H) terminated in the presence of water (e.g., Eggleston, 1999; Eggleston et al., 2003), but we have chosen the Fe termination for its consistency with the two magnetite surfaces, also Fe terminated. The Fe termination of hematite (001) is comprised of a 1/3 monolayer of Fe atoms overlying a close-packed oxygen plane (Fig. 2). Because of the low fractional occupation of all possible iron surface sites on these terminations, the uppermost iron Fe atoms are highly accessible to solvent water molecules and are here treated as protrusions into the overlying water phase. The surface plane is designated as the plane below, which is the uppermost plane of O atoms (the zero-plane in electrical double layer parlance). This also yields a surface plane definition satisfactorily unambiguous across
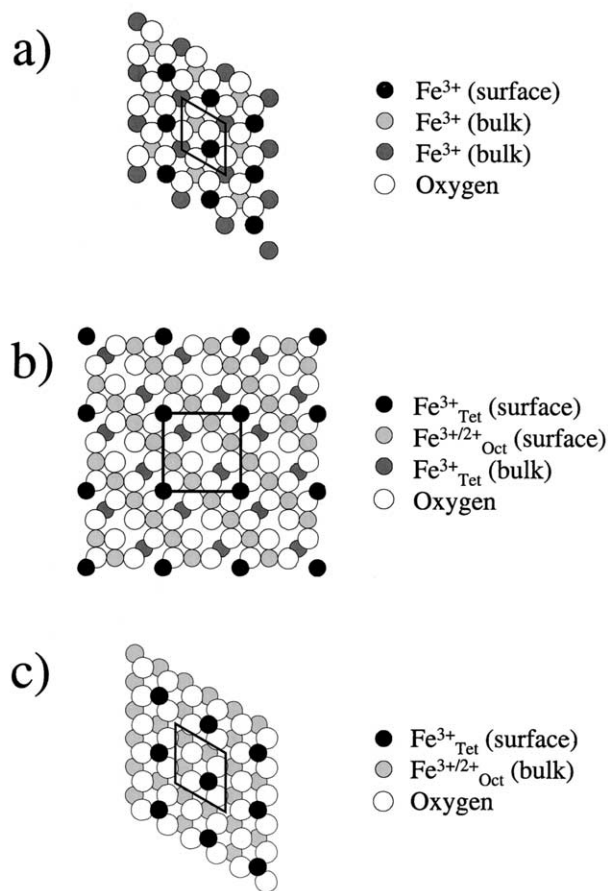

Fig. 2. Ball models of the surface structures of (a) hematite (001), (b) magnetite (100), and (c) magnetite (111) as viewed down the surface normal direction. Only the uppermost oxygen plane is shown along with Fe atoms coordinated to it. The tetrahedral and octahedral Fe sublattices in magnetite are differentiated by subscripts. The octahedral Fe sublattice in magnetite consists of equal numbers of 2+ and 3+ valence states.

the three surface types. An adsorbed water monolayer has been assumed for each surface, at a coverage of one H_2O molecule per uppermost Fe surface atom (Wasserman et al., 1997). For consistency, bulk spacings have been assumed for all three surfaces as the relaxed surface structures of magnetite are currently unavailable. We also note that the presence of overlying water tends to restore relaxed surface structures towards prerelaxed (i.e., bulk-like) configurations (Becker et al., 1996; Noguera, 1996).

The use here of DFT calculations to compute Marcus parameters is similar to previously described methods (Rosso and Rustad, 2000; Rosso and Morgan, 2002; Eggleston et al., 2003; Rosso et al., 2003a). The reorganization energy λ is separable into internal (λ_I) and external (λ_E) components. The internal component contains the energy required to reorganize bonds in the donor/acceptor centers to the configuration appropriate for electron transfer. The external component contains the energy required to change the polarization of the surrounding material to the configuration appropriate for electron transfer. The total reorganization energy (λ) is equal to $\lambda_I + \lambda_E$ (Marcus, 1956). The internal component for OmcA was taken as pertaining to an individual heme group. The heme group consists of a six-fold coordinated Fe atom in the plane of a protoporphyin ring providing four bonds and two axial ligands providing the other two bonds. Based on a major review of c-type cytochrome ET reactions, a radius of 5 Å for the heme group was assigned (Marcus and Sutin, 1985). Self-exchange electron transfer reactions indicate that λ_I is approximately 0.083 eV, computed as the

average of values reported by Marcus and Sutin (1985) and Fedurco (2000).

The internal reorganization energy for Fe(III) sites in the near-surface regions of hematite and magnetite were computed using DFT calculations and the 4-point method (Nelsen et al., 1987; Klimkans and Larsson, 1994; Rosso and Rustad, 2000; Rosso and Morgan, 2002; Eggleston et al., 2003; Rosso et al., 2003a) and molecular clusters excised from the bulk and surface structures (Fig. 3). More details of this method for hematite (001) surfaces can be found in Eggleston et al. (2003). Briefly, molecular clusters were excised from the surface structures described above for each unique Fe(III) site in the near-surface region. The clusters were chosen in such a way that local site geometry was preserved as best as possible while keeping the size of each cluster to less than ~20 Fe and O atoms for reasons of computational expense. The clusters were charge neutralized by saturating "dangling bonds" with protons using bond angles consistent with local symmetry around each site as found in surface. The clusters do not necessarily have to constitute stable "stand alone" molecular entities, but must capture the local bonding geometry and mimic bond lengths reasonably well. Magnetic structures were applied to the clusters that are consistent with the known magnetic structures in the bulk materials. DFT "breathing" optimizations of all bond lengths in each cluster were performed, followed by unconstrained geometry optimizations of the Fe site of interest in both the 3+ and 2+ valence states along with any sorbed water molecules that may be needed in specific cases (to accommodate the assumed sorbed water monolayer mentioned earlier). Single point energies were computed to acquire the vertical ionization potentials for the reduced Fe(II) configurations, and the vertical electron affinities for oxidized Fe(III) configurations. These calculations provided the four total energies for each cluster needed for a direct estimate of λ_{is} (Klimkans and Larsson, 1994). We used gaussian98 (Frisch et al., 1998) at the spin-unrestricted B3LYP level (Becke, 1993; Lee et al., 1988) using the Pople-type $6-311+G$ basis set (Wachters, 1970; Hay, 1977; Clark, 1983) to perform these calculations.

A diagram depicting the overall interfacial model used to compute the ET rates in this study is shown in Figure 4. For ET from a heme in OmcA to any Fe(III) surface site, we use the Marcus cross relation, $\lambda_{12} = \dfrac{(\lambda_{11} + \lambda_{22})}{2}$ to compute the internal component of the reorganization energy, where λ_{11} and λ_{22} are internal reorganization energies for hypothetical self-exchange reactions of the separate redox couples (Marcus and Sutin, 1985). We calculate λ_{os} using continuum equations derived by Marcus (1956, 1990). For Fe sites lying above or within the uppermost O plane, we used the continuum equation for ET in a single medium (Marcus, 1956)

$$\lambda_{os} = (\Delta q^2)\left(\frac{1}{2r_1} + \frac{1}{2r_2} - \frac{1}{R}\right)\left(\frac{1}{D_{op}} - \frac{1}{D_s}\right) \quad (8)$$

where q is the charge transferred, r_1 and r_2 are the effective radii of the reactant cavities (a surface Fe site and heme center), R is the ET distance (taken here as $r_1 + r_2 = R$), D_{op} is the optical dielectric constant of the medium (equals the index of refraction squared), and D_s is the static dielectric constant of the medium. For cases where ET is to deeper Fe sites, we use the expanded version of Eqn. 8 given for ET across an interface between two different dielectric materials (Marcus, 1990, eqn. 16). In all cases, we took the dielectric properties of the phase overlying the oxide surfaces as having $D_{op} = 2$ and $D_s = 10$, as is appropriate for the protein/water environment surrounding the heme groups in cytochrome c (Marcus and Sutin, 1985). This is based in part upon known properties of proteins, in part on the known decrease in the dielectric constant of water as water dipoles order at solid surfaces (e.g., Bockris and Reddy, 1973; Brown et al., 1999). The room temperature static dielectric constants for single crystal magnetite and hematite are not well known. For magnetite, D_s has been reported over a wide range from metallic-like ($D_s = 20000$, Shannon, 1993) to insulator-like ($D_s = 10$, Schlegel et al., 1979). A $D_s = 25$ was reported for hematite (Shannon, 1993). Because both hematite and magnetite are small polaron semiconductors we choose values for D_s that are more consistent with each other ($D_s = 10$ for magnetite and $D_s = 25$ for hematite), as incisively recommended by one of the manuscript reviewers. Likewise, we use an index of refraction of 3 ($D_{op} \sim n^2 = 9$) for both magnetite and hematite (Ehlers, 1987). The size of the cavity surrounding Fe sites in hematite was taken at 2.1 Å, approximating Fe(III)-O bond lengths. For all three oxide surfaces, the electron donating heme center of the hypothetical cytochrome c molecule was assigned a position directly above an uppermost Fe site at distance d (Fig. 4). For each determination of the total ET rate at a fixed d, the radius R was increased until all Fe(III) sites that made a significant contribution to the total rate were included.

The driving force for ET, $\Delta G^{0\prime}$, was estimated as the difference between the measured midpoint reduction potential for OmcA and the energy of the bottom of the conduction bands of magnetite and hematite as reconciled with the normal hydrogen electrode (NHE) scale at the pH of the experiments performed in this study (pH 7). OmcA has two sets of near-isopotential components at -0.243 V and -0.324 V with relative weights of 30 and 70% respectively (Field et al., 2000). We used the weighted average (-0.30 V) as the midpoint redox potential for OmcA. The conduction band minima (CBMs) for magnetite and hematite are pH-dependent and were determined as follows. The CBM of single crystalline hematite has been determined to lie at -0.44 V vs. NHE at pH 12 (Quinn et al., 1976). This value shifts linearly toward more positive values with decreasing pH by 0.059 V per unit pH change (Leland and Bard, 1987). Thus, at pH 7, the hematite CBM lies at -0.14 V vs. NHE. We assume n-type behavior for the hematite as is commonly observed and take the CBM to lie 0.1 V above the Fermi level (Leland and Bard, 1987). The magnetite CBM is less well known, but is known to lie at a different energy from hematite based upon X-ray absorption spectra (Pavicevic et al., 1993). According to Xu and Schoonen (2000), at pH 7, the CBM for magnetite would lie 0.17 V more negative than the CBM for hematite with the n-type character described above. Therefore, we take the magnetite CBM to lie at -0.30 V vs. NHE. Thus, the driving force for ET from OmcA to hematite is slightly energetically downhill and to magnetite it is very close to zero.

The quantity H_{AB} was computed as the geometric mean of the self-exchange H_{AB} terms for Fe(II/III) and cytochrome c at the particular ET distance R. H_{AB} varies with distance as (Newton and Sutin, 1984):

$$H_{AB} = H_{AB}^0 \exp\left[-\beta\left(r - r_0\right)\right] \quad (9)$$

where H_{AB}^0 is for the effective ET distance r_0 and β is the decay parameter. H_{AB}^0 for cytochrome c self-exchange ($r_0 = 6.4$ Å, Marcus and Sutin, 1985) was calculated using

$$\frac{2\pi}{\hbar} \frac{H_{AB}^2}{(4\pi\lambda RT)^{0.5}} \approx \kappa\nu \quad (10)$$

where $\kappa\nu$ and λ are known to be approximately 5×10^9 s^{-1} and 1 eV, respectively (Marcus and Sutin, 1985). The decay parameter was taken as 1.2 Å^{-1} for OmcA (Logan and Newton, 1983; Marcus and Sutin, 1985). H_{AB}, r_0, and β for Fe sites lying above the uppermost O plane were taken from directly computed values for corner-to-corner self-exchange reactions of the type:

$$Fe(OH_2)_6^{2+} + Fe(OH_2)_6^{3+} \rightarrow Fe(OH_2)_6^{3+} + Fe(OH_2)_6^{2+}$$
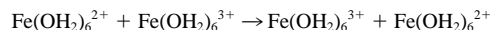
The corner-to-corner ET geometry mimics that expected at the uppermost Fe sites, each solvated by one overlying water molecule. For Fe sites deeper in the near-surface region, we used values consistent with bulk ET in hematite ($H_{AB}^0 = 1649$ cm^{-1}, $\beta = 1.2$ Å^{-1}, $r_0 = 3$ Å) (Rosso et al., 2003a).

3. RESULTS

3.1. Confirmation of Iron Reduction at the Mineral Surface

Surfaces which had been exposed to *S. oneidensis* MR-1 were compared to otherwise identical surfaces which were not exposed to *S. oneidensis* MR-1 to confirm that biologic reduction of the surface had indeed taken place. Multiplet splitting models were employed to determine the contribution of both ferric and ferrous ions to the Fe $2p_{3/2}$ core region (see Methods
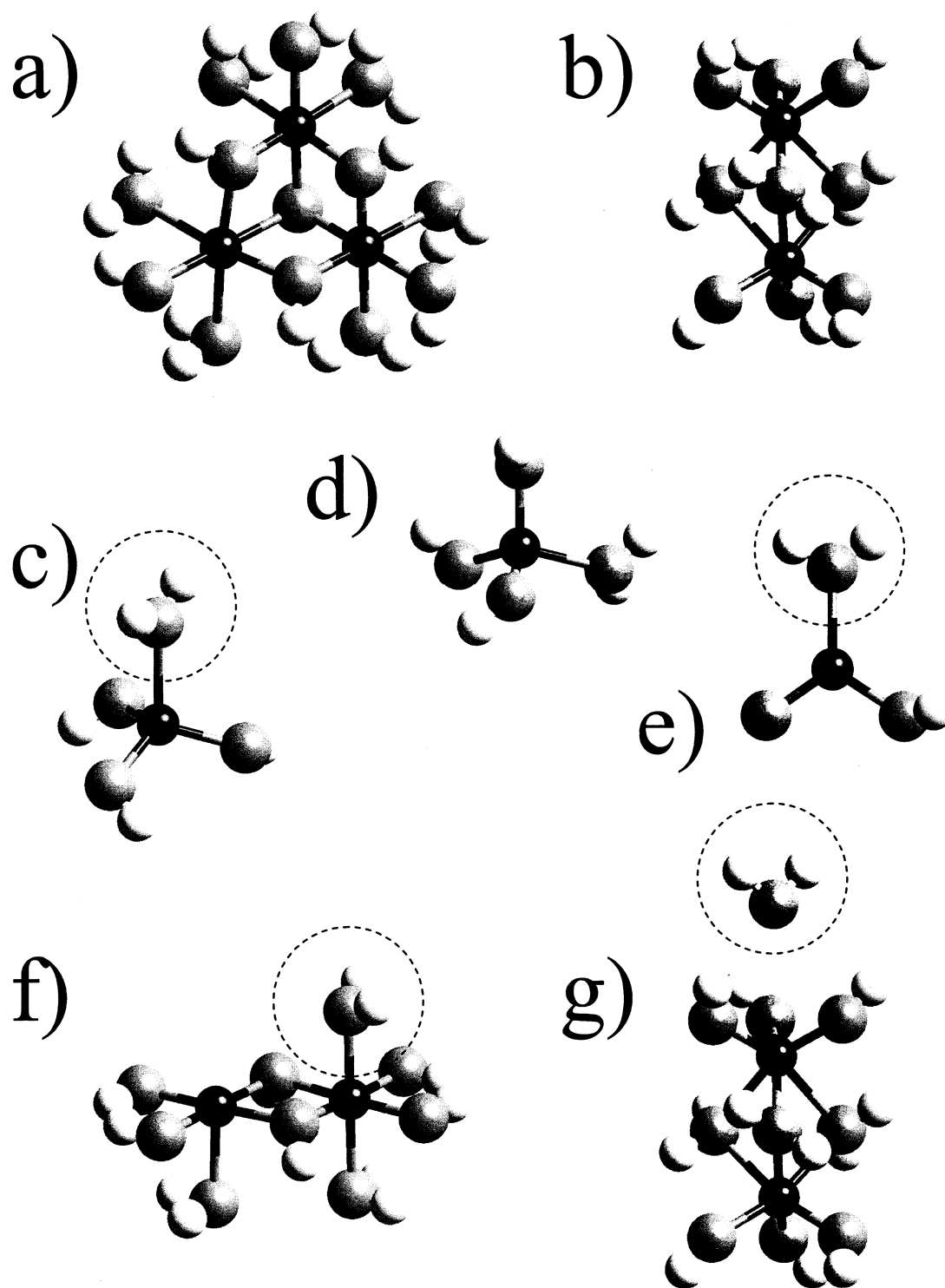
Fig. 3. Cluster models used to represent various bulk and surface sites for hematite and magnetite for inner-sphere reorganization energy calculations (see Methods section). Clusters were excised from experimentally determined bulk structures and excess charge was saturated with symmetry-preserving hydrogen atoms. A single water molecule was added to surface sites, denoted by dashed circles, to mimic a specifically sorbed water monolayer at the surface. (a) $Fe^{2+}Fe_2^{3+}$ trimer for bulk magnetite, (b) Fe_2^{3+} dimer for bulk hematite, (c) water-capped trigonal Fe^{3+} site for the hematite (001) and magnetite (111) surface, (d) tetrahedral Fe^{3+} for bulk magnetite, (e) water-capped tetrahedral Fe^{3+} for the magnetite (100) surface, (f) water-capped octahedral $Fe^{2+}Fe^{3+}$ dimer for the magnetite (100) surface, (g) water-capped Fe_2^{3+} dimer for the hematite (001) surface.
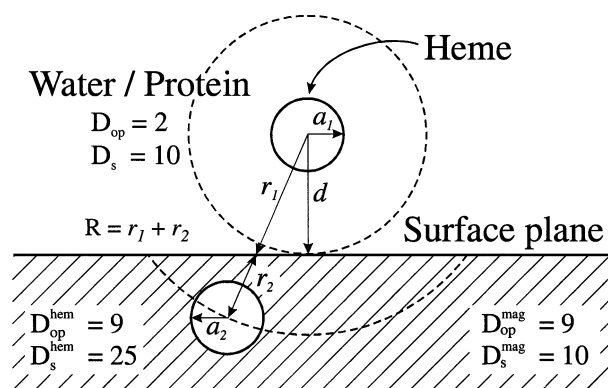
Fig. 4. Diagram of the general scheme used to model electron transfer from a heme of OmcA to the underlying oxide surfaces. Electron transfers to all possible Fe^{3+} acceptor sites were modeled individually for a given location of the overlying heme at a distance d from the uppermost oxygen plane. The heme radius a_1 (5 Å) and dielectric properties of the surrounding protein and near-surface water were taken from Marcus and Sutin (1985). For each Fe^{3+} acceptor site inner-sphere reorganization energies for acceptor sites were computed using DFT. The acceptor site cavity radius a_2 was defined as the average Fe-O bond length. The outer-sphere reorganization energies for material outside of cavities defined by a_1 and a_2 was treated using Marcus' continuum equations. The final rate was computed from a summation of all significant individual rates. More details are provided in the Methods section.

section). Figure 5 demonstrates the core photoelectron spectra and fitted multiplet photopeaks. The spectrum collected from the hematite surface exposed to growth medium in the absence of cells (Fig. 5a) is consistent with a monovalent Fe(III)-structure with a principle multiplet peak at 710.5 eV and five multiplet peaks of 1.4 eV full width at half maximum (FWHM) indicated as dashed component curves (McIntyre and Zetaruk, 1977; Junta-Rosso and Hochella, 1996). The spectrum collected from hematite following exposure to cells in growth medium clearly exhibits a contribution at lower binding energy (<710 eV) consistent with Fe(II) which is modeled by multiplet peaks with a principal binding energy of 709.3 eV (FWHM = 1.3 eV) and a satellite peak at 717.8 eV, indicated as solid component curves (Fig. 5b). A weak Fe(II) contribution is also evident in the spectrum collected from the magnetite (100) surface exposed to bacteria-free growth medium (Fig. 5c) at 709.2 eV (FWHM = 1.3eV). Hydration of the surface during exposure to growth medium is likely to result in the non-stoichiometric Fe(II) contribution. However, following exposure to cells (Fig. 5d) a significant Fe(II) contribution was observed with a principal multiplet peak at 709.3 eV (FWHM = 1.3 eV). Similar results were observed on the magnetite (111) surfaces (not shown). Clearly, exposure of these iron oxide surfaces to cells produced a significant Fe(II) component observable by XPS which was not present when surfaces were exposed to growth medium alone. Thus, this ferrous component appears to arise from reduction of the oxide surfaces by *S. oneidensis* MR-1.

3.2. Iron Oxide Surface-Associated Cell Accumulation

Following inoculation, cell densities on all three iron oxide faces were observed to increase with time (Fig. 6). A number of

different potential models were used to describe the cell accumulation data, in each case, highest coefficients of determination (r^2) were achieved by employing a sigmoid model. No a priori assumptions were made over the use of this model, which was simply used to provide parameters facilitating comparison between the three surfaces. The data of two trials on each surface were combined and successfully described by asymmetric sigmoid curves having first established there to be no significant difference between the two within-surface trials. It is immediately evident from the cell accumulation curves shown in Figure 6 that there are clear differences in maximum cell density (D_{max}) observed on the three faces. D_{max} observed on the hematite face was $6.367 \pm 0.328 \times 10^4$ cells cm^{-2} (mean $\pm$ standard error), significantly ($\alpha = 0.05$) greater than that observed on the more densely populated of the two magnetite faces, (111) with D_{max} of $4.040 \pm 0.267 \times 10^4$ cells cm^{-2} ($\Delta = 2.327 \times 10^4$ cells cm^{-2}; $t = 10.925$, $p < 0.001$). A significant difference in D_{max} was also observed between the magnetite (111) and magnetite (100) ($D_{max} = 3.446 \pm 0.251 \times 10^4$ cells cm^{-2}) faces ($\Delta = 0.594 \times 10^4$ cells cm^{-2}; $t = 3.246$, $p = 0.002$).

The rate of surface-associated cell accumulation (μ) across the three faces was more consistent. A maximum μ was observed on magnetite (111) ($\mu = 15.653 \pm 2.910$ cells cm^{-2} min^{-1}), not significantly different from that observed on hematite ($\mu = 12.665 \pm 1.879$ cells cm^{-2} min^{-1}, $\Delta = 2.988$ cells cm^{-2} min^{-1}; $t = 0.863$, $p = 0.392$). The difference between μ observed on hematite and magnetite (100) ($\mu = 8.331 \pm 1.900$ cells cm^{-2} min^{-1}) also proved non-significant ($\Delta = 4.334$ cells cm^{-2} min^{-1}; $t = 1.622$, $p = 0.102$). There was however, a significant difference between the two magnetite faces ($\Delta = 7.322$ cells cm^{-2} min^{-1}; $t = 2.107$, $p = 0.040$).

Silicon surfaces exposed to a culture of *S. oneidensis* MR-1 did not support cell accumulation. Following an initial cell density of 1.454×10^4 cells cm^{-2} at inoculation, cell numbers decreased until after 5 d and cell density on the Si surface was 0.672×10^4 cells cm^{-2} (data not shown).

3.3. Rate of Cell Detachment from Mineral Faces

Instantaneous cell detachment rates for the three faces increased with time and differed between the three faces. The high variability observed precludes any meaningful statistical analysis and the curves shown in Figure 7a should be considered as trends only. The relative increase in instantaneous cell detachment rate on the two magnetite faces is greater than on the hematite face, at the conclusion of the experiments there were more cells detaching from the magnetite faces than the hematite despite these faces having significantly reduced maximum surface-associated cell densities. The greater cell detachment rate observed on magnetite (111) is consistent with that face having the greatest surface-associated cell accumulation rate, while magnetite (100) and hematite have more similar instantaneous detachment rates and surface-associated cell accumulation rates.

3.4. Production of Cells at Mineral Faces

Assessment of total cell productivity derived from summing the total number of cells on each surface with the instantaneous cell detachment rate is shown in Figure 7b. Detached cells
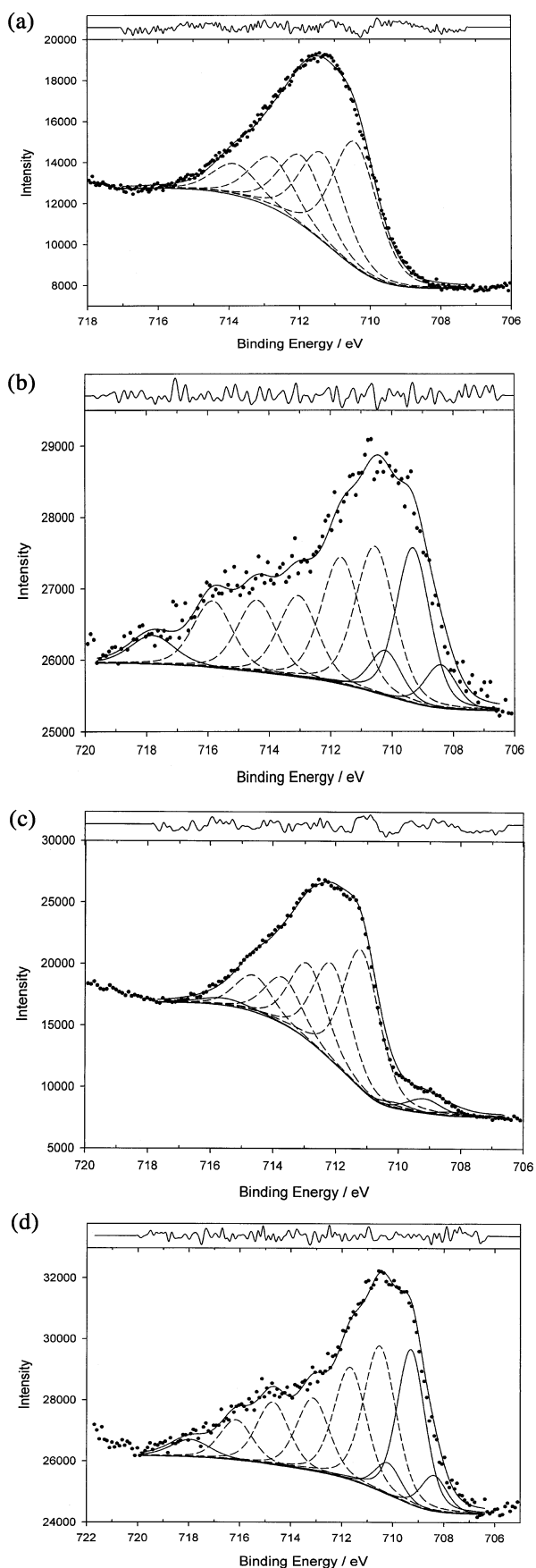
represent an important contribution to total productivity. Despite there being a statistically significant difference in the maximum cell density between the hematite (001) and magnetite (111) surfaces, with hematite supporting the greater cell density, once the number of cells detaching from the surface are accounted for there is very little difference between total productivity on the two faces. Overall, magnetite (100) supports the lowest surface-associated cell density and total productivity and represents a comparatively poor surface for growth of iron reducing bacteria. However, the fact that total cell productivity on hematite (001) and magnetite (111) is similar despite there being a significant difference in total cell density on the mineral surface suggests that the contribution of released cells to total cell productivity is surface dependent.

3.5. Theoretical Rates of ET

Calculated ET parameters and values of k (s^{-1}) for ET from an OmcA heme at various distances from the oxide surfaces to some of the important surface and near-surface Fe(III) sites are given in Table 1. The locations of most of the Fe sites are indicated in the surface structure diagrams in Figure 2. The heme/surface distances important for the current system are estimated to be in the range 5–9 Å as will be explained later in the discussion section.

Several important predictions are evident from the ET model. Because of the differing bonding geometries around the various sites, internal reorganization energies vary considerably (Table 1, parameter λ_I). Larger internal reorganization energies are primarily associated with the surface sites because of more degrees of freedom are available to the surface sites to modify the structure of their coordination spheres in response to reduction to Fe(II), and the inclusion of sorbed water, which is also free to move in response to reduction of a site to Fe(II). Internal reorganization energies for the bulk sites are smaller because of the geometric constraints imposed upon them by the surrounding structure. External reorganization energies (Table 1, parameter λ_E) are smaller for Fe sites at or above the uppermost O plane as distances to the donor heme center are considerably shorter, and because the dielectric properties of the protein surrounding the heme are somewhat different than that in the oxides themselves. The electronic coupling quantity H_{AB} tends to be very small (<10 cm^{-1}) for ET to bulk sites because of the long distances for ET overall (Table 1). Appreciable electronic coupling is only predicted for ET to uppermost surface Fe sites at the shorter end of the range of anticipated ET distances (≤ 5 Å, see "Discussion" below). The majority of the H_{AB} values are all significantly less than the conventional adiabatic threshold of ~ 200 cm^{-1} (Gratzel, 1989), justifying the non-adiabatic (weak-mixing) treatment applied here (see Methods section).

Fig. 5. Fe $2p$ core X-ray photoelectron spectra collected from hematite (001) surfaces, (a) exposed to sterile growth medium and (b) colonized by *S. oneidensis*, and magnetite (111) surfaces, (c) exposed to sterile growth medium and (d) colonized by *S. oneidensis*. Experimental data are shown as individual points. Multiplet peak contributions due to Fe(III) (dashed component curves) and Fe(II) (solid component curves) are shown together with the sum of the modeled curves and the residuals of the fit of the model to the experimental data (shown above the spectrum). C $1s$ = 284.8 eV.
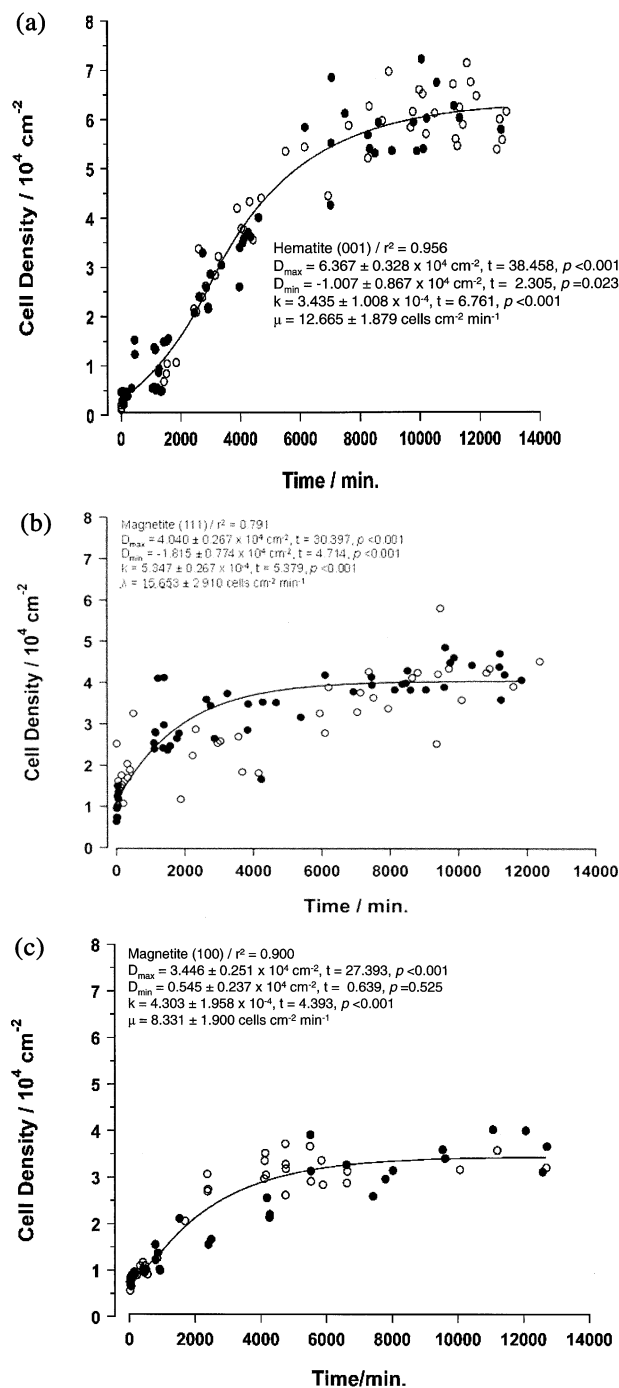
(a)

Hematite (001) / r² = 0.956
D_{max} = 6.367 ± 0.328 x 10⁴ cm⁻², t = 38.458, p <0.001
D_{min} = -1.007 ± 0.867 x 10⁴ cm⁻², t = 2.305, p =0.023
k = 3.435 ± 1.008 x 10⁻⁴, t = 6.761, p <0.001
μ = 12.665 ± 1.879 cells cm⁻² min⁻¹

(b)

Magnetite (111) / r² = 0.791
D_{max} = 4.040 ± 0.267 x 10⁴ cm⁻², t = 30.397, p <0.001
D_{min} = -1.815 ± 0.774 x 10⁴ cm⁻², t = 4.714, p <0.001
k = 5.947 ± 0.267 x 10⁻⁴, t = 5.379, p <0.001
μ = 15.653 ± 2.910 cells cm⁻² min⁻¹

(c)

Magnetite (100) / r² = 0.900
D_{max} = 3.446 ± 0.251 x 10⁴ cm⁻², t = 27.393, p <0.001
D_{min} = 0.545 ± 0.237 x 10⁴ cm⁻², t = 0.639, p =0.525
k = 4.303 ± 1.958 x 10⁻⁴, t = 4.393, p <0.001
μ = 8.331 ± 1.900 cells cm⁻² min⁻¹

Fig. 6. Accumulation of *S. oneidensis* cells on (a) hematite (001), (b) magnetite (111) and (c) magnetite (100) crystal faces. Closed and open data points represent the data from two independent growth experiments on each face. A common sigmoidal curve was fitted to the combined data on each face and the fitted curve parameters are given. Cell density was assessed from epifluorescent images of the GFP labeled cells in situ.

The ET behavior predicted for the three surfaces over a range of ET distances is shown in Figure 8. The decay in the log of the total ET rate as a function of increasing separation is similar for the three surfaces and is approximately linear as
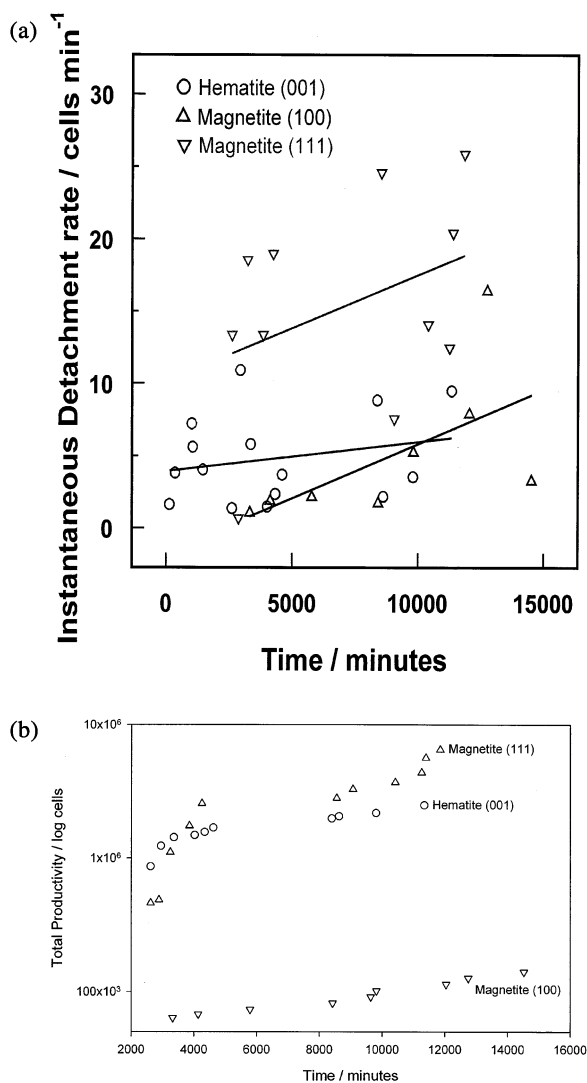
(a)

(b)

Fig. 7. (a) Instantaneous cell detachment rates measured over the time course of one experiment on each crystal face. Calculation of Instantaneous detachment rate is described in section 2.7. The lines in the figure describe the trends in the data only and do not reflect a statistical description of the data. (b) Total cell productivity derived from summing total number of cells on each surface and the instantaneous cell detachment rate.

expected from the Marcus theory treatment. The ET rate to hematite surfaces is predicted to be the fastest over the entire distance range considered. ET to magnetite (111) is consistently about two orders of magnitude slower than to hematite over the distance range, with magnetite (100) falling in the middle range with a unique distance dependence. The ET sequence which associates greater rates to hematite compared to either magnetite surface is consistent with the experimentally determined trend for the D_{max}. The model prediction that the ET rate is higher for magnetite (100) than for magnetite (111) is counter to that observed for D_{max} on the two crystal faces. In this respect, D_{max} and other descriptors of cell productivity on the two magnetite faces are more closely related to the Fe(III) site density where magnetite (111) has the higher density.

Table 1. Calculated heterogeneous electron transfer parameters for the reduction of various individual model Fe^{3+} sites in the near-surface of hematite (001), magnetite (111) and (100) by OmcA. The sites chosen for this table are those closest to the heme group location over the surface. Total electron transfer rates are computed by a summation of rates over all possible Fe^{3+} surface sites in near-surface region for each oxide surface.

Site	λ_I (eV)	$d = 5$ Å			$d = 6$ Å			$d = 7$ Å		
		λ_E (eV)	H_{AB} (cm^{-1})	$\log k$ (s^{-1})	λ_E (eV)	H_{AB} (cm^{-1})	$\log k$ (s^{-1})	λ_E (eV)	H_{AB} (cm^{-1})	$\log k$ (s^{-1})
Hem(001)										
Fe^{3+} (surf.)	0.47	0.55	823	12.0	0.82	179	9.5	1.00	39	7.4
Fe^{3+} (bulk)	0.27	1.96	9	2.5	2.04	3	1.2	2.11	1	−0.1
Mag (111)										
Fe^{3+}_{Tet} (surf.)	0.47	0.60	63	10.2	0.85	139	7.8	1.02	30	5.7
$Fe^{2+/2+}_{Oct}$ (surf.)	0.19	1.59	7	2.6	1.67	2	1.3	1.73	1	0.0
Fe^{3+}_{Tet} (bulk)	0.18	1.54	0	0.3	1.60	0	−1.0	1.65	0	−2.2
$Fe^{3+/2+}_{Oct}$ (bulk)	0.01	1.50	2	2.1	1.58	1	0.7	1.63	0	−0.5
Mag (100)										
Fe^{3+}_{Tet} (surf.)	0.39	0.48	1123	11.9	0.77	244	8.8	0.97	53	6.6
$Fe^{3+/2+}_{Oct}$ (surf.)	2.04	0.97	49	2.9	1.09	13	1.3	1.19	3	−0.3
Fe^{3+}_{Tet} (bulk)	0.18	1.51	4	2.5	1.59	1	1.1	1.65	0	−0.2
$Fe^{3+/2+}_{Oct}$ (bulk)	0.01	1.60	7	3.0	1.68	2	1.7	1.74	1	0.4

4. DISCUSSION

A sequential increase in maximum cell densities supported by the three mineral faces is observed with magnetite (100) sustaining the lowest, magnetite (111) an intermediate and hematite (001) a significantly greater density (Fig. 6). This sequence was not reflected in the number of cells collected in the effluent where, relatively, the two magnetite surfaces were associated with the greatest effluent cell density although high variability in the data precluded any attribution of statistical significance to the differences. Thus despite having similar surface areas, differences between cell accumulation at the surface and cells released into solution are observed between the three crystal faces. The mode of growth of *S. oneidensis* on hematite appears to be surface related; on magnetite proportionately more daughter cells leave the surface. However, total cell productivity on the magnetite (100) surface is much re-

Fig. 8. Total electron transfer rates (Eqn. 6) computed as a function of the distance of separation d between the heme and oxygen plane of the surfaces (Fig. 4). The range of electron transfer distances of relevance to the interfacial system in this study is 5–9 Å (see text for discussion).

duced compared to the other two faces, consistent with this face supporting the lowest surface-associated population.

Whilst magnetite (100) clearly represents the poorest surface for cell accumulation and productivity, differences between magnetite (111) and hematite (001) are less apparent. Although hematite (001) supports the highest surface-associated population, the rate of accumulation (μ) of this population is intermediate between that observed on magnetite (111), which exhibits the highest μ, and magnetite (100) which exhibits the lowest (see section 3.2). Furthermore the total cell productivities associated with hematite (001) and magnetite (111) surfaces are very similar (Fig. 7b). Thus the various measures of cell "activity" employed here all suggest that the magnetite (100) face is very dissimilar from the other two faces.

It is envisioned that at least three primary processes are occurring at the interface between cells and oxide surfaces during sustained bioreduction, ET to Fe(III) sites, release of Fe(II) as a soluble phase and regeneration of the oxide surface, and/or accumulation of Fe(II) at the mineral surface in a secondary solid phase. As mentioned above, evidence was found for the reduction of surface Fe(III) to Fe(II) and its accumulation at the mineral/cell surface. There are also poorly understood issues concerning what happens to electrons once they have been transferred to the oxide surface (i.e., electron mobility) and how donated electrons are spatially and kinetically linked with release of Fe(II) from the solid surface. Because of differences in the surface structures, these processes will undoubtedly differ among the various oxide surfaces, forming a basis, wholly or in part, for the differences in cell accumulation rates and productivity that we observed. Although most of these molecular-scale issues are amenable to theoretical modeling, addressing all of them in the current study was not feasible. Rather, here we have focused molecular modeling on the question of whether or not the rate of ET to the surface can be a possible basis for discriminating the surface-specific cell growth behavior observed.
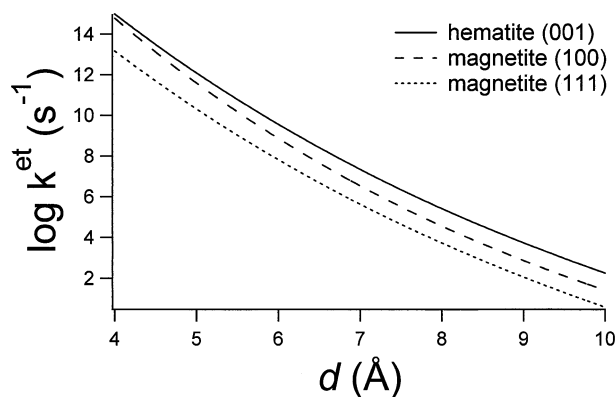
The ET modeling predictions show that kinetics should be

strongly dependent on both the surface structure and on the distance of separation between a heme center in OmcA and the oxide surface. Several lines of evidence suggest heme/surface distances pertinent to the current system fall in the range 5–9 Å. Heme centers are asymmetrically distributed in the protein envelope in the interior of cytochrome c molecules, with heme Fe atoms typically 13–14 Å from the protein surface (Fedurco, 2000). However, mixing of the Fe t_{2g} orbitals with the π^* system of the porphyrin ring typically extends the metal d-orbital electron density to the ring edge, effectively reducing distances for ET via heme edges (Marcus and Sutin, 1985). Intermolecular edge-to-edge distances in encounter complexes for ET reactions between cytochrome c molecules are predicted to be between 9–10 Å (Marcus and Sutin, 1985; Wendoloski et al., 1987). Therefore, we anticipate that a minimum distance of separation between a heme edge and a bare oxide surface is half that range, or ~5 Å with a maximum of 7 Å. Introducing a monolayer of specifically chemisorbed water molecules at the oxide surface increases the height of the heme over the Fe acceptor sites of the surface by ~2 Å (Eggleston et al., 2003). Therefore, the maximum electron transfer distance of interest, under the assumption of "hard-shell" contact (i.e., no unaccounted for intervening material) is 9 Å for OmcA in contact with a surface covered with a monolayer of water.

ET to hematite (001) is predicted to be faster than to magnetite surfaces over a much larger range of distances (Fig. 8). Hence, it seems possible that the rate at which cells can directly transfer electrons to the oxide surface exerts an influence upon the maximum cell density. However, the predicted ET rates are contrary to the observed trend in D_{max} within the subset of the two magnetite surfaces. The current state of knowledge about the details of the ET process and interfacial structure at the cell-oxide contact is poor; we are therefore unable to discriminate between model failure and a lack of correlation between the predicted k^{et} and measured D_{max}. Our ET model is approximate in a number of ways and we view it more as a stepping-off point for future calculations of this nature. However, the ET model is reliably consistent with the experimental observations in that surface structure is an important factor for this interfacial system.

The ET model also points to the importance of the presence of the uppermost Fe atoms overlying the topmost O plane at all three surfaces. These Fe atoms have the opportunity to strongly couple electronically with donor heme groups juxtaposed the surface. They also dominate the electron accepting capacity for ET distances at the shorter end of the range considered here. For example, adjusting our model for hematite (001) by removing the uppermost Fe atoms, ET rates for Fe- versus O-terminations of hematite (001) can be compared. For an ET distance of 5 Å, ET from OmcA to the Fe-termination is predicted to be nine orders of magnitude faster than for the O-termination. At 10 Å, the difference is reduced by five orders of magnitude. At longer distances the difference continues to narrow, reflecting the diminishing importance of the uppermost Fe atoms.

Discrepancy between modeling and observation on the two magnetite surfaces would suggest that our efforts have not accounted for all differences between surfaces likely to influence growth. We have chosen to model electron transfer because intuitively, it would seem to have a direct effect upon the ability of iron-reducing bacteria to grow. What we have not

accounted for, however, is the effect of subsequent chemical changes at the oxide surfaces such as the formation of passive layers or secondary mineral phases which may hamper continued ET to the oxide surface. Here we allude to the ferrous ion, which has a clear inhibitory effect upon continued reduction (and therefore growth) at iron oxide surfaces (Roden and Urrutia, 2002). This leaves the question as to the relative influence of the Fe(III)-site density upon observed cell productivity. Calculated site density decreases from 4.2 nm^{-2} on hematite (001) to 1.4 nm^{-2} on magnetite (100) (Fig. 2). Magnetite (111) exhibits an intermediate site density of 2.8 nm^{-2}. Thus, the increase in site density across the three surfaces mirrors the observed trend for D_{max}, but is not borne out by the ET model, suggesting that Fe(III) site density alone is an overly simplistic metric for the electron-accepting ability of a surface. It is thus difficult to separate the effects and clearly, conceptually the rate of dissimilatory iron reduction (and thus cell productivity) will reflect both. If site density is of greater significance at lower rates of ET, this may explain the fact that productivity is so reduced on magnetite (100) faces. However, assuming an effective bacterium-surface contact area on an ideally flat surface to be 300 nm^2 (Edwards and Rutenberg, 2001), a cell attached to magnetite (100) would have the potential to transfer electrons to approximately 420 Fe(III) sites within the near-surface region. Since the absolute minimum ET rate required to sustain cellular growth is unknown further conjecture is unprofitable. Hematite, with the highest density of Fe(III)-sites and rate of electron transfer exhibits the highest D_{max}, although there is no significant difference between μ measured on hematite (001) and magnetite (111) there is a significant reduction in D_{max} consistent with reductions both in Fe(III)-site density and ET rate. This difference is not observed in the total cell productivity however, because a greater proportion of daughter cells leave the magnetite (111) surface than the hematite (001) surface. A shift from surface- to solution-associated growth is evident. Once site densities and ET rates fall to those observed on magnetite (100) both D_{max} and μ are significantly reduced resulting in the observed reduction in total cell productivity in an apparently interactive effect. Clearly, this initial study does not allow discrimination between effects of Fe(III) site density and ET rates upon D_{max} and μ. However, the experimental observations, as well as ET modeling predictions concur on our central premise that surface structure is an important factor for this interfacial system. From a biogeochemical perspective therefore, whilst mineral surface area has profound influence upon the rate of reduction of iron minerals, other properties of the surface cannot be ignored and at some, as yet, undetermined scale the surface physiochemistry may be a significant factor in determining rates of mineral reduction and cell growth.

Considerations of those properties determining the relative reactivity of iron oxides and hydroxides in soil and subsurface environments usually focus on surface area and degree of crystallinity, stemming largely from commonly observed correlations between these factors, and reactivity. However, reactivity series inconsistent with surface area and/or crystallinity have been observed suggesting that other properties of iron minerals also affect the relative reduction rates. Here, we have tested the hypothesis that bioreactivity is in part controlled by the atomic and electronic structural properties of the electron accepting solid surface. Three different iron oxide single crystal

surfaces were employed to study their relative intrinsic biore-activity towards *S. oneidensis* under controlled surface area conditions. Although we have not studied Fe(III) reduction rates directly, we have followed cell accumulation and detachment rates at the three surfaces and inferred "reactivity" from total cell productivity. By assessing and combining both accumulation and detachment data we are able to better assess differences between the three surfaces. The observations show a clear dependence of bioreactivity on the surface structure. Molecular modeling of direct electron transfer rates from a model outer membrane cytochrome to the three iron oxide surfaces has been performed. The model demonstrates the impact of surface structure on ET, an important part of the respiration process. This supports the conclusion that differences between the surfaces in the observed production rates arise from differences in the properties of the electron acceptor. Therefore, in the absence of any direct method of assessing ET from bacterial cells to mineral surfaces, we have been able to implicate surface structure as a factor likely to be responsible for determining cell activity.

REFERENCES

Arnold R. G., DiChristina T. J., and Hoffman M. R. (1988) Reductive dissolution of Fe(III) oxides by *Pseudomonas* sp. 200. *Biotech. Bioeng.* **32,** 1081–1096.

Banwart S., Davies S., and Stumm W. (1989) The role of oxalate in accelerating the reductive dissolution of hematite (α-Fe$_2$O$_3$) by ascorbate. *Colloids Surf.* **39,** 303–309.

Baty A. M. III, Eastburn C. C., Techarnjanaruk S., Goodman A. E., and Geesey G. G. (2000) Spatial and temporal variations in chitinolytic gene expression and biomass production during chitin degradation. *Appl. Environ. Microbiol.* **66,** 3574–3585.

Becke A. D. (1993) A new mixing of Hartree-Fock and local density functional theories. *J. Chem. Phys.* **98,** 1372–1377.

Becker U., Hochella M. F., and Apra E. (1996) The electronic structure of hematite (001) surfaces: Applications to the interpretation of STM images and heterogeneous surface reactions. *Am. Min.* **81,** 1301–1314.

Beliaev A. S., Saffarini D. A., McLaughlin J. L., and Hunnicutt D. (2001) MtrC, an outer membrane decaheme c cytochrome required for metal reduction in *Shewanella putrefaciens* MR-1. *Mol. Microbiol.* **39,** 722–730.

Bockris J. O. M. and Reddy A. K. N. (1973) *Modern Electrochemistry.* Plenum Press.

Canfield D. E. (1989) Reactive iron in marine sediments. *Geochim. Cosmochim. Acta* **53,** 619–659.

Canfield D. E., Raiswell R., and Bottrell S. (1992) The reactivity of sedimentary iron minerals towards sulfide. *Am. J. Sci.* **292,** 659–683.

Casella G. and Berger R. L. (1990) *Statistical Inference.* Wadsworth & Brooks/Cole Advanced Books and Software.

Chambers S. A., Thevuthasan S., and Joyce S. A. (2000) Surface structure of MBE-grown Fe$_3$O$_4$ (001) by X-ray photoelectron diffraction and scanning tunneling microscopy. *Surf. Sci.* **450,** L273–L279.

Clark T., Chandrasekhar J., Spitznagel G. W., and Schleyer P. V. (1983) Efficient diffuse function augmented basis sets for anion calculations. III. The 3–21+G basis set for 1st-row elements, Li-F. *J. Comp. Chem.* **4,** 294–301.

Cornell R. M. and Schwertmann U. (1996) *The Iron Oxides: Structure, Properties, Reactions, Occurrence and Uses.* VCH.

Das A. and Caccavo F. (2000) Fe(III) oxide reduction by *Shewanella alga* BrY requires adhesion. *Curr. Microbiol.* **40,** 344–347.

Dong H., Fredrickson J. K., Kennedy D. W., Zachara J. M., Kukkadapu R. K., and Onstott T. (2000) Mineral transformation associated with the microbial reduction of magnetite. *Chem. Geol.* **169,** 299–318.

dos Santos Afonso M. and Stumm W. (1992) Reductive dissolution of iron(III) hydr(oxides) by hydrogen sulfide. *Langmiur* **8,** 1671–1675.

Edwards K. J. and Rutenberg A. D. (2001) Microbial response to surface microtopography: The role of metabolism in localized mineral dissolution. *Chem. Geol.* **180,** 19–32.

Eggleston C. M. (1999) The surface structure of α-Fe$_2$O$_3$ (001) by scanning tunneling microscopy: Implications for interfacial electron transfer reactions. *Am. Mineral.* **84,** 1061–1070.

Eggleston C. M., Stack A. G., Rosso K. M., Higgins S. R., Bice A. M., Boese S. W., Pribyl R. D., and Nichols J. J. (2003) The structure of hematite (α-Fe$_2$O$_3$) (001) surfaces in aqueous media: Scanning tunneling microscopy and resonant tunneling calculations of coexisting O and Fe terminations. *Geochim. Cosmochim. Acta* **67,** 985–1000.

Ehlers E. G. (1987) *Optical Mineralogy: Mineral Descriptions.* Blackwell Scientific.

Fedurco M. (2000) Redox reactions of heme-containing metalloproteins: Dynamic effects of self-assembled monolayers on thermodynamics and kinetics of cytochrome c electron-transfer reactions. *Coord. Chem. Rev.* **209,** 263–331.

Field S. J., Dobbin P. S., Cheesman M. R., Watmough N. J., Thomson A. J., and Richardson D. J. (2000) Purification and magneto-optical spectroscopic characterization of cytoplasmic membrane and outer membrane multiheme c-type cytochromes from *Shewanella frigidimarina* NCIMB400. *J. Biol. Chem.* **275,** 8515–8522.

Fischer W. R. (1988) Microbiological reactions of iron in soils. In *Iron in Soils and Clay Minerals* (eds. J. W. Stucki, B. A. Goodman, and U Schwertmann), pp. 715–748. NATO ASI Series 217. D. Reidel.

Fredrickson J. K., Zachara J. M., Kennedy D. W., Dong H., Onstott T. C., Hinman N. W., and Li S. M. (1998) Biogenic iron mineralization accompanying the dissimilatory reduction of hydrous ferric oxide by a ground water bacterium. *Geochim. Cosmochim. Acta* **62,** 3239–3257.

Frisch M. J., Trucks G. W., Schlegel H. B., Scuseria J. A., Robb M. A., Cheeseman J. R., Zakrzewski V. G., Montgomery J. A., Stratmann R. E., Burant J. C., Dapprich S., Millam J. M., Daniels A. D., Kudin K. N., Strain M. C., Farkas O., Tomasi J., Barone V., Cossi M., Cammi R., Mennucci B., Pomelli C., Adamo C., Clifford S., Ochterski J., Petersson G. A., Ayala P. Y., Cui Q., Morokuma K., Malick D. K., Rabuck A. D., Raghavachari K., Foresman J. B., Cioslowski J., Ortiz J. V., Stefanov B. B., Liu G., Liashenko A., Piskorz P., Komaromi I., Gomperts R., Martin R. L., Fox D. J., Keith T., Al-Laham M. A., Peng C. Y., Nanayakkara A., Gonzalez C., Challacombe M., Gill P. M. W., Johnson B., Chen W., Wong M. W., Andres J. L., Gonzalez C., Head-Gordon M., Replogle E. S., and Pople J. A. (1998) *Gaussian98* (Revision A.4). Gaussian Inc.

Gao Y. Q., Georgievskii Y., Marcus R. A., and Noyes Laboratory of Chemical Physics CIoTPCA USA (2000) On the theory of electron transfer reactions at semiconductor electrode/liquid interfaces. *J. Chem. Phys.* **112,** 3358–3369.

Goodenough J. B. (1971) Metallic oxides. In *Progress in Solid State Chemistry*, Vol. 5 (ed. H. Reiss), pp. 149–399. Pergamon Press.

Gratzel M. (1989) *Heterogeneous Photochemical Electron Transfer.* CRC Press.

Gupta R. P. and Sen S. K. (1974) Calculation of multiplet structure of core *p*-vacancy levels. *Phys. Rev. B* **10,** 71–77.

Gupta R. P. and Sen S. K. (1975) Calculation of multiplet structure of core *p*-vacancy levels. II. *Phys. Rev. B* **12,** 15–19.

Hay P. J. (1977) Gaussian basis sets for molecular calculations. The representation of 3d orbitals in transition-metal atoms. *J. Chem. Phys.* **66,** 4377.

Herbert R. B., Benner S. G., Pratt A. R., and Blowes D. W. (1998) Surface chemistry and morphology of poorly crystalline iron sulfides precipitated in media containing sulfate. *Chem. Geol.* **144,** 87–97.

Jones J. G., Gardener S., and Simon B. M. (1983) Bacterial reduction of ferric iron in a stratified eutrophic lake. *J. Gen. Microbiol.* **129,** 131–139.

Junta-Rosso J. L. and Hochella M. F. (1996) The chemistry of hematite {001} surfaces. *Am. Mineral.* **60,** 305–314.

Klimkans A. and Larsson S. (1994) Reorganization energies in benzene, naphthalene, and anthracene. *Chem. Phys.* **189,** 25–31.

Kostka J. E., Stucki J. W., Nealson K. H., and Wu J. (1996) Reduction of structural Fe(III) in smectite by a pure culture of *Shewanella putrefaciens* strain MR-1. *Clays Clay Miner.* **44,** 522–529.

Kostka J. E. and Nealson K. H. (1998) Isolation, cultivation and characterization of iron- and manganese-reducing bacteria. In *Techniques in Microbial Ecology* (eds. R. S. Burlage, R. Atlas, D. Stahl, G. G. Geesey, and G. Sayler), pp. 58–78. Oxford University Press.

Kostka J. E., Wu J., Nealson K. H., and Stucki J. W. (1999) The impact of structural Fe(III) reduction by bacteria on the surface chemistry of smectite clay minerals. *Geochim. Cosmochim. Acta* **63,** 3705–3713.

Landa E. R., Phillips E. J. P., and Lovely D. R. (1991) Release of ^{226}Ra from uranium mill tailings by microbial Fe(III) reduction. *Appl. Geochem.* **6,** 647–652.

Lee C. T., Yang W. T., and Parr R. G. (1988) Development of the Colle-Salvetti correlation energy formula into a functional of the electron density. *Phys. Rev. B* **37,** 785–789.

Leland J. K. and Bard A. J. (1987) Photochemistry of colloidal semiconducting iron oxide polymorphs. *J. Phys. Chem.* **91,** 5076–5083.

Logan J. and Newton M. D. (1983) Ab initio study of electronic coupling in the aqueous Fe^{2+}-Fe^{3+} electron exchange process. *J. Chem. Phys.* **78,** 4086–4091.

Lovely D. R. (1991) Dissimilatory Fe(III) and Mn(IV) reduction. *Microbiol. Rev.* **55,** 1472–1480.

Lovely D. R., Stolz J. F., Nord J. L., and Phillips E. J. P. (1987) Anaerobic production of magnetite by a dissimilatory iron-reducing microorganism. *Nature* **330,** 252–254.

Lovley D. R., Coates J. D., Blunt-Harris E. L., Phillips E. J. P., and Woodward J. C. (1996) Humic substances as electron acceptors for microbial respiration. *Nature* **382,** 445–448.

Lovley D. R., Fraga J. L., Blunt-Harris E. L., Hayes L. A., Phillips E. J. P., and Coates J. D. (1998) Humic substances as a mediator for microbially catalyzed metal reduction. *Acta Hydrochim. Hydrobiol.* **26,** 152–157.

Lower S. K., Hochella M. F., and Beveridge T. J. (2001) Bacterial recognition of mineral surfaces: Nanoscale interactions between *Shewanella* and α-FeOOH. *Science* **292,** 1360–1363.

Marcus R. A. (1956) On the theory of oxidation-reduction reactions involving electron transfer. *J. Chem. Phys.* **24,** 966–978.

Marcus R. A. (1990) Reorganization free energy for electron transfers at liquid-liquid and dielectric semiconductor-liquid interfaces. *J. Phys. Chem.* **94,** 1050–1055.

Marcus R. A. and Sutin N. (1985) Electron transfers in chemistry and biology. *Biochim. Biophys. Acta* **811,** 265–322.

McIntyre N. S. and Zetaruk D. G. (1977) X-ray photoelectron spectroscopic studies of iron oxides. *Anal. Chem.* **49,** 1521–1529.

Morse J. W. and Wang Q. (1997) Pyrite formation under conditions approximating those in anoxic sediments: II. Influence of precursor iron minerals and organic matter. *Chem. Geol.* **57,** 187–193.

Munch J. C. and Ottow J. C. G. (1980) Preferential reduction of amorphous to crystalline iron oxides by bacteria activity. *Soil Sci.* **129,** 1–21.

Myers J. M. and Myers C. R. (1998) Isolation and sequence of OmcA, a gene encoding a decaheme outer membrane cytochrome c of *Shewanella putrefaciens* MR-1, and detection of OmcA homologs in

other strains of *S. putrefaciens*. *Biochim. Biophys. Acta-Biomem.* **1373,** 237–251.

Myers J. M. and Myers C. R. (2001) Role for outer membrane cytochromes OmcA and OmcB of *Shewanella putrefaciens* MR-1 in reduction of manganese dioxide. *Appl. Envron. Microbiol.* **67,** 260–269.

Neal A. L., Teckarnjanaruk S., Dohnalkova A., McCreedy D., Peyton B. M., and Geesey G. G. (2001) Iron sulfides and sulfur species produced at hematite surfaces in the presence of sulfate-reducing bacteria. *Geochim. Cosmochim. Acta* **65,** 223–235.

Nealson K. H. and Saffarini D. A. (1995) Iron and manganese in anaerobic respiration: Environmental significance, physiology, and regulation. *Annu. Rev. Microbiol.* **48,** 311–343.

Nealson K. H. and Little B. (1997) Breathing manganese and iron: Solid-state respiration. *Adv. Appl. Microbiol.* **45,** 213–239.

Nebe-von Caron G. and Badley R. A. (1996) Bacterial characterization by flow cytometry. In *Flow Cytometry Applications in Cell Culture* (eds. M. Al-Rubeai and A. N. Emery), pp. 241–290. Marcel Dekker.

Nelsen S. F., Blackstock S. C., and Kim Y. (1987) Estimation of inner shell Marcus terms for amino nitrogen compounds by molecular orbital calculations. *J. Am. Chem. Soc.* **109,** 677–682.

Newman D. K. and Kolter R. (2000) A role for excreted quinones in extracellular electron transfer. *Nature* **405,** 94–97.

Newton M. D. and Sutin N. (1984) Electron transfer reactions in condensed phases. *Ann. Rev. Phys. Chem.* **35,** 437–480.

Noguera C. (1996) *Physics and Chemistry at Oxide Surfaces.* Cambridge University Press.

Pavicevic M. K., Timotijevic D., and Amthauer G. (1993) Electron configuration of the valence and the conduction band of magnetite (Fe_3O_4) and hematite (α-Fe_2O_3). *Inst. Phys. Conf. Ser.* **130,** 101–104.

Postma D. (1993) The reactivity of iron oxides in sediments: A kinetic approach. *Geochim. Cosmochim. Acta* **57,** 5027–5034.

Pratt A. R., Muir I. J., and Nesbitt H. W. (1994a) X-ray photoelectron and Auger electron spectroscopic studies of pyrrhotite and mechanism of air oxidation. *Geochim. Cosmochim. Acta* **58,** 827–841.

Pratt A. R., Nesbitt H. W., and Muir I. J. (1994b) Generation of acids from mine waste: Oxidative leaching of pyrrhotite in dilute H_2SO_4 solutions at pH 3.0. *Geochim. Cosmochim. Acta* **58,** 5417–5159.

Quinn R. K., Nasby R. D., and Baughman R. J. (1976) Photoassisted electrolysis of water using single crystal α-Fe_2O_3 anodes. *J. Mater. Res. Bull.* **11,** 1011.

Ritter M. and Weiss W. (1999) Fe_3O_4(111) surface structure determined by LEED crystallography. *Surf. Sci.* **432,** 81–94.

Roden E. E. and Zachara J. M. (1996) Microbial reduction of crystalline Fe(III) oxides: Influence of oxide surface area and potential for cell growth. *Environ. Sci. Technol.* **30,** 1618–1628.

Roden E. E. and Urrutia M. M. (2002) Influence of biogenic Fe(II) on bacterial crystalline Fe(III) oxide reduction. *Geomicrobiol. J.* **19,** 209–251.

Rosso K. M. and Rustad J. R. (2000) Ab initio calculation of homogeneous outer sphere electron transfer rates: Application to $M(OH_2)_6^{3+/2+}$ redox couples. *J. Phys. Chem. A* **104,** 6718–6725.

Rosso K. M. and Morgan J. J. (2002) Outer-sphere electron transfer kinetics of metal ion oxidation by molecular oxygen. *Geochim. Cosmochim. Acta* **66,** 4223–4233.

Rosso K. M., Smith D. M. A., and Dupuis M. (2003a) An ab initio model of electron transport in hematite (α-Fe_2O_3) basal planes. *J. Chem. Phys.* **118,** 6455–6466.

Rosso K. M., Zachara J. M., Fredrickson J. K., Gorby Y. A., and Smith S. C. (2003b) Non-local bacterial electron transfer to hematite surfaces. *Geochim. Cosmochim. Acta* **67,** 1081–1087.

Schlegel A., Alvarado S. F., and Wachter P. (1979) Optical properties of magnetite (Fe_3O_4). *J. Phys. C Sol. State Phys.* **12,** 1157–1164.

Shannon R. D. (1993) Dielectric Polarizabilities of Ions in Oxides and Fluorides. *J. Appl. Phys.* **73,** 348–366.

Sherman D. M. (1987) Molecular orbital (SCF-X-a-SW) theory of metal-metal charge transfer processes in minerals. 1. Application to Fe^{2+}-Fe^{3+} charge transfer and electron delocalization in mixed valence iron oxides and silicates. *Phys. Chem. Min.* **14,** 355–363.

Shirley D. A. (1972) High-resolution X-ray photoelectron spectrum of the valence bands of gold. *Phys. Rev. B* **5,** 4709–4714.

Sidhu P. S., Gilkes R. J., Cornell R. M., Posner A. M., and Quirk J. P. (1981) Dissolution of iron oxides and oxyhydroxides in hydrochloric and perchloric acids. *Clays Clay Miner.* **29,** 269–276.

Turick C. E., Tisa L. S., and Caccavo F. (2002) Melanin production and use as a soluble electron shuttle for Fe(III) oxide reduction and as a terminal electron acceptor by *Shewanella algae* BrY. *Appl. Environ. Microbiol.* **68,** 2436–2444.

Venkateswaran K., Moser D. P., Dollhopf M. E., Lies D. P., Saffarini D. A., MacGregor B. J., Ringelberg D. B., White D. C., Nishijima M., Sano H., Burghardt J., Stackebrandt E., and Nealson K. H. (1999) Polyphasic taxonomy of the genus *Shewanella* and description of *Shewanella oneidensis* sp. nov. *Int. J. Syst. Bacteriol.* **49,** 705–724.

Vives-Rego J., Lebaron P., and Nebe-von Caron G. (2000) Current and future applications of flow cytometry in aquatic microbiology. *FEMS Microbiol. Rev.* **24,** 429–448.

Wachters A. J. H. (1970) Gaussian basis set for molecular wavefunctions containing third-row atoms. *J. Chem. Phys.* **52,** 1033.

Wasserman E., Rustad J. R., Felmy A. R., Hay B. P., and Halley J. W. (1997) Ewald methods for polarizable surfaces with application to hydroxylation and hydrogen bonding on the (012) and (001)surfaces of α-Fe_2O_3. *Surf. Sci.* **385,** 217–239.

Wendoloski J. J., Matthew J. B., Weber P. C., and Salemme F. R. (1987) Molecular dynamics of a cytochrome-C cytochrome-B5 electron transfer complex. *Science* **238,** 794–797.

Xu Y. and Schoonen M. A. A. (2000) The absolute energy positions of conduction and valence bands of selected semiconducting minerals. *Am. Mineral.* **85,** 543–556.

Zachara J. M., Fredrickson J. K., Li S.-M., Kennedy D. W., Smith S. C., and Gassman P. L. (1998) Bacterial reduction of crystalline Fe^{3+} oxides in single phase suspensions and subsurface materials. *Am. Mineral.* **83,** 1426–1443.

Zinder B., Furrer G., and Stumm W. (1986) The coordination chemistry of weathering: II. Dissolution of Fe(III) oxides. *Geochim. Cosmochim. Acta* **50,** 1861–1869.